The Astrophysical Journal, 842:132 (15pp), 2017 June 20 https://doi.org/10.3847/1538-4357/aa75cc

Joining X-Ray to Lensing: An Accurate Combined Analysis of MACS J0416.1–2403

M. Bonamigo[1], C. Grillo[1,2], S. Ettori[3,4], G. B. Caminha[5], P. Rosati[5], A. Mercurio[6], M. Annunziatella[7], I. Balestra[8], and M. Lombardi[2]
[1] Dark Cosmology Centre, Niels Bohr Institute, University of Copenhagen, Juliane Maries Vej 30, DK-2100 Copenhagen, Denmark; bonamigo@dark-cosmology.dk
[2] Dipartimento di Fisica, Università degli Studi di Milano, via Celoria 16, I-20133 Milano, Italy
[3] INAF, Osservatorio Astronomico di Bologna, Via Piero Gobetti, 93/3, 40129 Bologna, Italy
[4] INFN, Sezione di Bologna, viale Berti Pichat 6/2, I-40127 Bologna, Italy
[5] Dipartimento di Fisica e Scienze della Terra, Università degli Studi di Ferrara, Via Saragat 1, I-44122 Ferrara, Italy
[6] INAF—Osservatorio Astronomico di Capodimonte, Via Moiariello 16, I-80131 Napoli, Italy
[7] INAF—Osservatorio Astronomico di Trieste, Via G.B. Tiepolo, 11 I-34143 Trieste, Italy
[8] University Observatory Munich, Scheinerstrasse 1, D-81679 Munich, Germany
Received 2017 January 30; revised 2017 May 22; accepted 2017 May 27; published 2017 June 23

Abstract

We present a novel approach for a combined analysis of X-ray and gravitational lensing data and apply this technique to the merging galaxy cluster MACS J0416.1–2403. The method exploits the information on the intracluster gas distribution that comes from a fit of the X-ray surface brightness and then includes the hot gas as a fixed mass component in the strong-lensing analysis. With our new technique, we can separate the collisional from the collision-less diffuse mass components, thus obtaining a more accurate reconstruction of the dark matter distribution in the core of a cluster. We introduce an analytical description of the X-ray emission coming from a set of dual pseudo-isothermal elliptical mass distributions, which can be directly used in most lensing softwares. By combining *Chandra* observations with Hubble Frontier Fields imaging and Multi Unit Spectroscopic Explorer spectroscopy in MACS J0416.1–2403, we measure a projected gas-to-total mass fraction of approximately 10% at 350 kpc from the cluster center. Compared to the results of a more traditional cluster mass model (diffuse halos plus member galaxies), we find a significant difference in the cumulative projected mass profile of the dark matter component and that the dark matter over total mass fraction is almost constant, out to more than 350 kpc. In the coming era of large surveys, these results show the need of multiprobe analyses for detailed dark matter studies in galaxy clusters.

Key words: dark matter – galaxies: clusters: general – galaxies: clusters: individual (MACS J0416.1–2403) – gravitational lensing: strong – X-rays: galaxies: clusters

1. Introduction

Galaxy clusters are one of the most powerful and promising tools available for the study of the different mass components of the universe (Voit 2005; Jullo et al. 2010; Kneib & Natarajan 2011; Laureijs et al. 2011; Postman et al. 2012). They are the largest gravitationally bound objects in the sky, and as such, they represent a young population that formed only recently, in accordance with the hierarchical assembly predicted by the concordance cosmological model (e.g., Tormen 1997; Klypin et al. 1999; Moore et al. 1999; Springel et al. 2001). The late formation time of clusters makes their mass and number density distributions sensitive to the presence of dark energy, which only recently has been dominating the dynamical evolution of the universe. Galaxy clusters are also the strongest gravitational lenses, with dozens of families of observed multiple images of background sources (Broadhurst et al. 2005; Halkola et al. 2006). In addition, galaxy clusters host very hot gas halos arising from the infall of surrounding material into their deep potential wells (Sarazin 1988; Ettori et al. 2013). For these reasons, galaxy clusters have been targeted in many observational campaigns, using various techniques and facilities, to study their different mass components. For example, the Cluster Lensing And Supernova survey with Hubble (CLASH; Postman et al. 2012), the Hubble Frontier Fields (HFF; Lotz et al. 2017), and the Reionization Lensing Cluster Survey (RELICS[9]) have obtained multiband *Hubble Space Telescope* (*HST*) images, supplemented with ground-based telescope photometric and spectroscopic data, to map the cluster total mass distribution via strong and weak gravitational lensing. Targeted observations using X-ray telescopes, like *Chandra* and *XMM Newton*, and submillimeter (for the Sunyaev–Zel'dovich effect) and radio antennas have characterized the hot cluster gas component (e.g., Donahue et al. 2014; Ogrean et al. 2016; Rumsey et al. 2016; van Weeren et al. 2017). Thousands of member galaxies and multiply lensed images have been spectroscopically confirmed using the Visual Multi-Object Spectrograph (Le Fèvre et al. 2003), for the CLASH-VLT program (Rosati et al. 2014), and more recently the Multi Unit Spectroscopic Explorer (MUSE; Bacon et al. 2012) instruments at the VLT (e.g., Biviano et al. 2013; Karman et al. 2017; Monna et al. 2017). All these campaigns have helped to push further our understanding of the mass composition of galaxy clusters and the population of high-z sources. In particular, the HFF program has dedicated 140 *HST* orbits to each of the six massive clusters in the sample with the aim of enabling the study of the population of the highest-redshift galaxies, the first to undergo star formation, thanks to the magnification effect of the cluster lenses (e.g., Balestra et al. 2013; Coe et al. 2015; Oesch et al. 2015; Vanzella et al. 2017). Moreover, the HFF data represent an unprecedented opportunity to improve the lensing modeling of the clusters and thus to study in more detail the dark matter halos in which they live.

In this work, we focus on the galaxy cluster MACS J0416.1–2403 (hereafter MACS 0416), present in both the

[9] https://relics.stsci.edu/

CLASH and HFF samples and first discovered in the Massive Cluster Survey (MACS) by Mann & Ebeling (2012). MACS 0416 is located at $z_l = 0.396$ and has an M_{200} mass of approximately $9 \times 10^{14}\,M_{\odot}$ and an X-ray luminosity $L_X \approx 10^{45}$ erg s^{-1} (Balestra et al. 2016). The cluster hosts two brightest cluster galaxies (BCGs), G1 and G2, located, respectively, in its northeast (R.A. = 04:16:09.154, decl. = –24:04:02.90) and southwest (R.A. = 04:16:07.671, decl. = –24:04:38.75) regions. MACS 0416 is clearly undergoing a merging event, as is shown by its X-ray morphology and by the large separation (∼200 kpc) in projection of the two BCGs (Mann & Ebeling 2012).

Given its inclusion in the HFF sample and its high efficiency in magnifying background sources, MACS 0416 has been the target of many recent studies. After the first strong-lensing analysis by Zitrin et al. (2013), which identified 70 multiple images, Jauzac et al. (2014, 2015) combined strong- and weak-lensing data to model a total of 194 multiple images (almost all of them without spectroscopic confirmation). Additional works (Johnson et al. 2014; Richard et al. 2014; Diego et al. 2015) focused on this cluster and provided maps of its total mass and magnification factors. Exploiting the spectra obtained within the CLASH-VLT program (presented in Balestra et al. 2016), Grillo et al. (2015, hereafter Gr15) accurately modeled the positions of 30 multiple images, all from spectroscopically confirmed sources. More recently, Caminha et al. (2017, hereafter Ca17) used HFF and MUSE data to improve the lensing analysis by Gr15, extending the number of secure spectroscopic multiple images to 102 and making MACS 0416 the cluster with the largest number of spectroscopically confirmed multiple images known to date.

Complementing the gravitational lensing analysis of Gr15, Balestra et al. (2016) used X-ray data and the dynamics of approximately 800 member galaxies to independently measure the total mass of the cluster, finding a good agreement between the different mass diagnostics. Similarly, Jauzac et al. (2015) used X-ray data to model the hot gas distribution in order to clarify the merging history of MACS 0416. Both groups treated X-ray and strong-lensing data separately. Ideally, one would want to simultaneously fit the gravitational lensing and X-ray data, combining the individual likelihoods into a single value to maximize. This has been done by various authors, most recently by Morandi et al. (2012), Umetsu et al. (2015), Siegel et al. (2016), and Sereno et al. (2017); for a more detailed review on the subject see Limousin et al. (2013). However, the downside of the current implementations of this approach is that the lensing analysis is done separately and the observable that enters in the combined fit is the fixed, reconstructed total surface mass density. An alternative, and complementary, strategy is to measure the hot gas mass density from the X-ray surface brightness and then include it in a proper strong-lensing analysis that uses the positions of observed multiple images as constraints. This is the method we choose in the current paper to improve the strong gravitational lensing analysis of Ca17 by adding multiwavelength information from the X-ray emission of the hot intracluster gas. This approach has some advantages over a more traditional analysis, where the hot gas is subtracted a posteriori from the diffuse halo component. In particular, the inferred dark matter mass density distribution could differ because of the added constraints from the X-ray data. Moreover, a traditional analysis cannot measure the parameter values of the diffuse dark matter halo without the bias introduced by the hot intracluster gas. A similar technique has been attempted by Paraficz et al. (2016) in the Bullet cluster (1E 0657–56), where the large offset between the X-ray emission and the total mass distribution required the separate treatment of the hot gas component in the gravitational lensing analysis. The wealth of data available for MACS 0416 allows us here to adopt a much more accurate description for the hot gas and the other components of the cluster, for example, by modeling the spatial distribution of the X-ray emission beyond the approximation of a single mass density profile.

There are three main reasons to combine information from different mass diagnostics: first, any systematic effect (or absence of it) should become evident in the disagreement of the probes considered (Balestra et al. 2016); second, as the various data sets depend differently on each component, some degeneracies can be broken (for instance, projection effects; Limousin et al. 2013); lastly, a multiwavelength analysis can help separate the constituents of a cluster, allowing for a more detailed study of the individual components. This is key to testing the collisionless nature of dark matter in merging systems and the inner structure of dark matter halos predicted by the standard cold dark matter (CDM) model. For instance, in the presence of self-interacting dark matter (SIDM), the three main components of a cluster (dark matter, hot intracluster gas, and member galaxies) should exhibit a precise displacement after the first passage in a merging event (Markevitch et al. 2004; Harvey et al. 2015). The center of the galaxies' distribution, in each subcluster, should be located farther away from the overall barycenter, as they represent a fully noncollisional component that moves almost unperturbed through the cluster. The opposite behavior is characteristic of the hot intracluster gas, which, being a collisional fluid, is compressed and lags behind during the core passage. The center of an SIDM distribution should be found somewhere in the middle between the other two components. In principle, it is possible to constrain the cross section of SIDM from the offset between the center positions of the dark matter and galaxies' distributions (Markevitch et al. 2004; Harvey et al. 2015). We notice that in previous studies about MACS 0416 (e.g., Ogrean et al. 2015) only a very small displacement has been observed between the centers of the X-ray and optical luminosity peaks. This might be ascribed to the complex cluster merging geometry, which renders also an estimate of the dark matter cross section less straightforward. To this last particular aim, the technique presented here should be more effective in galaxy clusters with more favorable geometrical configurations.

The paper is organized as follows. In Section 2, we introduce the X-ray observations and the modeling technique used to estimate the hot intracluster gas. In Section 3, we briefly present the strong-lensing data and the adopted cluster mass models used in our analysis. Section 4 contains the results of the strong-lensing study, where the hot gas is treated as a separate and fixed mass component. Finally, in Section 5, we summarize our conclusions.

Throughout the paper, we adopt a flat ΛCDM cosmology with Hubble constant $H_0 = 70$ km s^{-1} Mpc^{-1} and total matter density $\Omega_m = 0.3$. At the redshift of the lens of $z_l = 0.396$, 1″

corresponds to 5.34 kpc in the assumed cosmology. All magnitudes are given in the AB system.

2. X-Ray Surface Brightness Analysis

In this section, we present our new technique to model the hot gas mass distribution of a cluster, and apply this method to MACS 0416.

2.1. X-Ray Surface Brightness from Dual Pseudo-isothermal Elliptical Mass Density Profiles

The X-ray surface brightness $S_X(x, y)$ of an object at redshift z_l is given by

$$S_X(x, y) = \frac{\Lambda(T, Z)}{4\pi(1 + z_l)^4} \int_{-\infty}^{+\infty} n_e(x, y, z) n_p(x, y, z) dz, \quad (1)$$

where $n_e(x, y, z)$ is the electron density, $n_p(x, y, z)$ is the proton density, Z is the metallicity of the gas, and $\Lambda(T, Z)$ is its cooling function (Boehringer & Hensler 1989; Sutherland & Dopita 1993).

Traditionally, two methods are used to derive the hot gas density from the X-ray surface brightness (see Ettori et al. 2013, and references therein): (1) by considering the geometry of the system, it is possible to deproject the surface brightness and obtain the gas density; (2) modeling the gas density and then projecting it allows one to fit the observed X-ray photon counts and thus infer the parameter values of the assumed gas distribution. In this work, we adopt the second approach (because the multipeak mass distribution of MACS 0416 makes a simple geometrical deprojection less suitable). Moreover, we explicitly seek an analytical description of the hot gas mass density distribution that can be easily included in strong-lensing models. To this aim, we adopt a dual pseudo-isothermal elliptical (dPIE) mass distribution (hereafter dPIE; Elíasdóttir et al. 2007; Suyu & Halkola 2010), largely used in strong-lensing analyses, instead of a β-model (Cavaliere & Fusco-Femiano 1976; Sarazin & Bahcall 1977), more common in X-ray studies, to describe the hot gas. The 3D mass density of a dPIE distribution, with vanishing ellipticity, can be expressed as (Limousin et al. 2005)

$$\rho(x, y, z) = \frac{\rho_0}{\left(1 + \frac{x^2+y^2+z^2}{R_C^2}\right)\left(1 + \frac{x^2+y^2+z^2}{R_T^2}\right)}, \quad (2)$$

where ρ_0 is the central density and R_C and R_T are the core and truncation radii, respectively. A dPIE distribution can be seen as a special case of the density profile introduced by Vikhlinin et al. (2006) as a generalization of the β-model. The value of ρ_0 is related to that of the normalization of the surface mass density, i.e., the "central velocity dispersion" σ_0 in Equation (10), via

$$\rho_0 = \frac{\sigma_0^2}{2\pi G}\left(\frac{R_C + R_T}{R_C^2 R_T}\right). \quad (3)$$

We notice that here the term "velocity dispersion" does not have a dynamical meaning and has to be considered only as an effective parameter. Hereafter, we will use the following substitutions:

$$\begin{cases} R_A^2 = R_C^2 + (x - x_0)^2 + (y - y_0)^2 \\ R_B^2 = R_T^2 + (x - x_0)^2 + (y - y_0)^2 \end{cases}, \quad (4)$$

thus shifting the center of the profile at the position (x_0, y_0) on the plane of the sky.

Neglecting constant factors, such as the conversion from electron and proton densities to gas density, and using Equation (2), we obtain the following analytical solution for the surface brightness shown in Equation (1):

$$\begin{aligned} S_X \propto \int_{-\infty}^{+\infty} \rho^2 dz &= \int_{-\infty}^{+\infty} \frac{\rho_0^2 R_C^4 R_T^4 dz}{(R_A^2 + z^2)^2 (R_B^2 + z^2)^2} \\ &= \frac{\pi \rho_0^2 R_C^4 R_T^4 (R_A^2 + 3R_A R_B + R_B^2)}{2R_A^3 R_B^3 (R_A + R_B)^3}. \end{aligned} \quad (5)$$

It is possible to generalize the problem to the situation where multiple components are present, but we need to assume that they all lie on the same plane along the line of sight to obtain an analytical result. The inclusion of a possible difference in z between separate gas components is beyond the scope of this analysis and not relevant for the strong-lensing analysis of MACS 0416. Within this single-plane assumption, the surface brightness of N dPIE components is proportional to

$$\int_{-\infty}^{+\infty} \rho^2 dz = \sum_{i=1}^{N} I_i(x, y) + 2\sum_{i \neq j}^{N} I_{i,j}(x, y), \quad (6)$$

where $I_i(x, y)$ is the solution to the one-component problem (in Equation (5)) and the second term $I_{i,j}(x, y)$ is

$$\begin{aligned} I_{i,j}(x, y) &= \int_{-\infty}^{+\infty} \rho_i \rho_j \, dz \\ &= \int_{-\infty}^{+\infty} \frac{(\rho_{0i} R_{Ci}^2 R_{Ti}^2)(\rho_{0j} R_{Cj}^2 R_{Tj}^2) dz}{(R_{Ai}^2 + z^2)(R_{Bi}^2 + z^2)(R_{Aj}^2 + z^2)(R_{Bj}^2 + z^2)} \\ &= \pi (\rho_{0i} R_{Ci}^2 R_{Ti}^2)(\rho_{0j} R_{Cj}^2 R_{Tj}^2) \frac{\alpha_{i,j}}{\beta_{i,j}}, \end{aligned} \quad (7)$$

where

$$\begin{aligned} \alpha_{i,j} = &(R_{Bi} + R_{Aj})(R_{Bi} + R_{Bj})(R_{Aj} + R_{Bj}) \\ &+ R_{Ai}(R_{Bi} + R_{Aj} + R_{Bj})^2 + R_{Ai}^2(R_{Bi} + R_{Aj} + R_{Bj}) \end{aligned} \quad (8)$$

and

$$\begin{aligned} \beta_{i,j} = &R_{Ai} R_{Bi} R_{Aj} R_{Bj} (R_{Ai} + R_{Bi})(R_{Ai} + R_{Aj}) \\ &\times (R_{Ai} + R_{Bj})(R_{Bi} + R_{Aj})(R_{Bi} + R_{Bj})(R_{Aj} + R_{Bj}). \end{aligned} \quad (9)$$

In Appendix B, we show the solution for the particular case of two components and also discuss a generalization beyond the spherically symmetric approximation.

From an X-ray-only fit, it is not possible to break the degeneracy between surface brightness normalization and elongation along the line of sight; therefore, the surface mass density measured under the spherical approximation is biased

by a factor that depends on the real geometry of the system. In the most unfavorable scenario of a prolate ellipsoid, with axis ratio s aligned with the line of sight, this factor is $1/\sqrt{s}$ (De Filippis et al. 2005). Without further information from other observables, though, this bias cannot be quantified in MACS 0416, especially given the extremely complex nature of this cluster.

2.2. X-Ray Surface Brightness Fit of MACS J0416.1–2403

First, we model the X-ray surface brightness of MACS 0416. We combine multiple *Chandra* observations (obsID: 16236, 16237, 16304, 16523, 17313; see Ogrean et al. 2015), for a total of 293 ks of exposure time, and reduce them using *CIAO 4.7* and *CALDB 4.6.9*. The resulting surface brightness map, limited in the energy range from 0.7 to 2 keV and corrected for exposure, is then binned to 8 times the pixel resolution of *Chandra*, obtaining a final pixel size of 3.″94. This pixel size is much larger than *Chandra*'s on-axis point-spread function; therefore, we do not consider this effect in our analysis.

From the modeling presented in the previous section, we can obtain the projected squared gas density (see Equation (6)). To convert this into an X-ray surface brightness, we use Equation (1), which requires us to estimate the cooling function. This, in turn, depends on the assumed mechanism of photon emission and on the temperature and metallicity of the gas. We use an Astrophysical Plasma Emission Code (APEC[10]) model for the X-ray emissivity, with the addition of a photoelectric absorption (phabs[11]) from the foreground galactic gas. For the latter, we adopt an equivalent column density of 3.04×10^{20} cm^{-2}, measured from the LAB Survey of Galactic HI (Kalberla et al. 2005) in a cone of radius 1° centered on MACS 0416. Finally, as the cooling function has only a weak dependence on the temperature T in the energy range considered in this work (Ettori 2000), we assume a constant gas temperature of 10.8 keV and a metallicity of 0.24, i.e., the median values measured from the *Chandra* data within a circle with radius of 2′. It is worth noticing that these temperature and metallicity values are extremely close to those of 10.06 keV and 0.24, estimated within a larger radius of 3.′75 by Ogrean et al. (2015). From these values, we can compute the photon rate for the intracluster hot gas.

A uniform background of 0.805 counts/pixel (similar to the value used in Ogrean et al. 2015) is then added to the model; this has been measured in a region of the image sufficiently far away (≈4′) from the cluster emission. We have checked that using a lower value for the background emission (i.e., 0.6 counts/pixel), or leaving it as a free parameter, does not change appreciably the value of the fitting figure of merit and results in a difference in the cumulative projected gas mass of at maximum 4% at 350 kpc from the cluster center.

To infer the values of the parameters of the model, we use the software *Sherpa*.[12] We adopt the Cash statistic C (Cash 1979) as the likelihood function, as this is more appropriate than a traditional Gaussian likelihood for the low counts of a Poisson distribution. We restrict the fit to the inner circular region with a radius equal to 40 image pixels (i.e., approximately 840 kpc) of the surface brightness map and mask all point sources, found with the *wavedetect* algorithm.

[10] http://atomdb.org/
[11] Xspec manual: phabs
[12] http://cxc.harvard.edu/sherpa

Table 1
Best-fitting Values of the Parameters of the Three-Component dPIE (with Vanishing Ellipticity) Model of the X-Ray Surface Brightness of MACS 0416

Parameter	Northeast 1	Northeast 2	Southwest
x_0 (″)	−30	−2	29
y_0 (″)	21	0	−50
σ_0 (km s^{-1})	317	201	328
R_C (″)	34	13	35
R_T (″)	$>5 \times 10^3$	>750	210

Note. Centers are relative to the northeast BCG, G1 (R.A. = 04:16:09.154, decl. = –24:04:02.90).

To satisfactorily describe the X-ray surface brightness of MACS 0416, we adopt a model that consists of three spherical dPIE components, with a resulting total surface brightness proportional to the expression given in Equation (6). Each of the three components has five free parameters: the position of the center, x_0 and y_0, the central velocity dispersion, σ_0, the core radius, R_C, and the truncation radius, R_T. Table 1 presents the best-fitting values of the parameters of the three dPIE components (the center coordinates are given with respect to the northern BCG). The final value of the adopted statistic is 6448, which corresponds to a reduced value of 1.31, given the 4914 degrees of freedom (dof) of the model.

The hot gas distribution of the cluster is well represented by two diffuse components (Northeast 1 and Southwest in Table 1) with values of central velocity dispersion of approximately 320 km s^{-1} and of core radius of about 180 kpc. The northeast clump requires an additional, more compact ($R_C \approx 70$ kpc) component with a central velocity dispersion value of approximately 200 km s^{-1}. All three dPIE components show very large values of R_T, extending beyond the radius of the fitted region. In passing, we note that for large values of R_T, a dPIE profile becomes very similar to a β-model profile in the central regions. The combination of the two northern components gives the total density for the main northeast gas clump, and neither of them corresponds to the third dPIE distribution needed in the lensing analysis (see 3.1). The relative positions of the northern components are noteworthy: the compact component is centered on the BCG, while the diffuse one is displaced by almost 200 kpc. This offset creates the asymmetric emission that is seen in the X-ray surface brightness in the first two columns of Figure 1, observations and models, respectively (see later a more detailed description of the figure). Such asymmetry was observed already by Ogrean et al. (2015) and can be tentatively interpreted as a tail formed as the subcluster approaches the first core passage in a merging scenario.

Interestingly, our centers of the two main components are in moderate agreement with the results of Jauzac et al. (2015), but they find that the northeast distribution has a core radius almost three times larger than the southwest one, while the values of our core radii are very similar and approximately equal to 180 kpc. The lack of information on the fitting procedure implemented in Jauzac et al. (2015), such as the size of the analyzed region, does not allow a more detailed comparison between the two works.

The addition of a third component is necessary to accurately reproduce the compact emission coming from the center of the northernmost clump, as can be clearly seen in Figure 1. Here

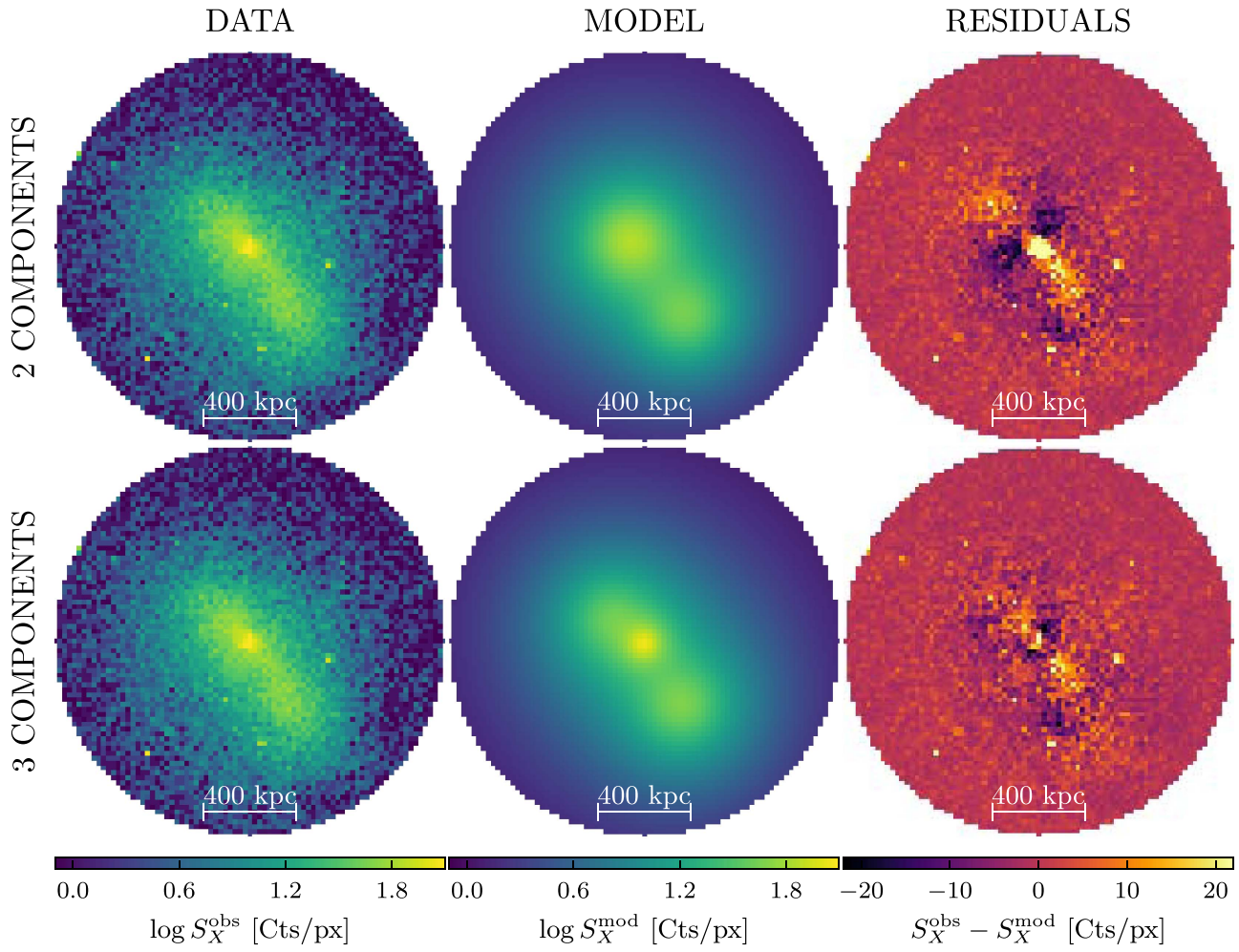

Figure 1. X-ray surface brightness (logarithmic scale) and residual maps of MACS 0416: observed counts (first column), best-fitting model (second column), and residuals (third column). The top and bottom rows show the maps for the two-component and three-component models, respectively. Each panel shows the circular region with a radius of 40 image pixels (i.e., ≈840 kpc) used in the fitting procedure. The point sources are shown only for graphical reasons and have been masked out in the fitting procedure.

we show data, model, and residuals of a two- and three-spherical-component model, in the top and bottom rows, respectively. The first two columns represent the logarithm of the photon counts of the observations and models, while the last one shows the residuals. It is evident that the two-component model cannot fit well, at the same time, the large-scale diffuse emission and the central compact peak. A similar result has been found by Ogrean et al. (2015), which used a double β-model to fit the northeast subcluster. A two-component model underpredicts the photon counts in the image inner regions, which correspond to the position of G1, the northern BCG. As a further test, we tried a model that consists only of two elliptical components: the fit continues to fail in representing the bright central peak of emission, and the reduced statistic did not improve compared to the three spherical mass distributions.

We summarize the results of these three different models in Table 2, where we show the degrees of freedom and the minimum value of the fitting Cash statistic C. Furthermore, we include the values of the Akaike information criterion (AIC; Akaike 1974) and Bayesian Information Criterion (BIC; Schwarz 1978), two quantities that are often used for model comparison. All of these criteria show that the three-spherical-component model is preferable to a two-component one, whether we include ellipticity or not.

Table 2
Comparison between Different Models for the Gas Distribution: Two Spherical, Two Elliptical, and Three Spherical dPIE Components

Model	dof	C	AIC	BIC
Two spherical dPIE	4919	7391	7411	7475
Two elliptical dPIE	4915	6817	6845	6936
Three spherical dPIE	4914	6448	6478	6575

Note. Columns show the degrees of freedom (dof), the minimum value of the fitting cash statistic C, the Akaike Information Criterion (AIC), and the Bayesian Information Criterion (BIC).

As a final check, in Figure 2 we have compared the cumulative projected gas mass profile of the best-fitting three-component model with that obtained by directly deprojecting the gas. The latter has been recovered through the geometrical deprojection (see, e.g., Ettori et al. 2013, and references therein) of the

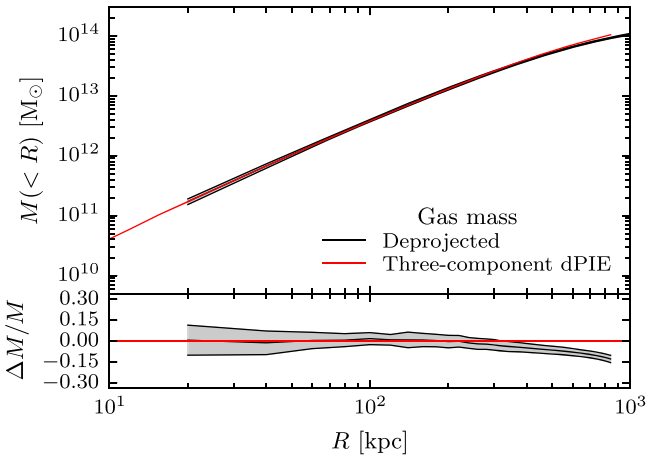

Figure 2. Top panel: cumulative projected gas mass profiles of MACS 0416. The red curve shows the best-fitting three-component dPIE model, while the central black curve shows the values obtained with a deprojection technique. The gray region, delimited by solid black curves, indicates the $\pm 1\sigma$ errors for the deprojected profile. Bottom panel: relative difference between the deprojected and three-component dPIE model gas mass profiles. The central curve shows the median values, while the gray region (delimited by solid black curves) shows the $\pm 1\sigma$ errors derived only from the deprojected profile uncertainties.

azimuthally averaged surface brightness profile that considers the entire X-ray emission, as described in Balestra et al. (2016; Appendix A). This 3D mass profile is then projected along the line of sight to estimate the quantity shown in Figure 2. The top panel of the figure shows the radial profiles as computed from the three-component dPIE model (red line) and from deprojecting the surface brightness (black line with 1σ errors shown as gray regions); the bottom panel, on the other hand, gives the relative difference between the two mass measurements. Errors in the bottom panel are derived only from the errors in the deprojected profile; therefore, they represent a lower limit of the uncertainties. The agreement between the two different methods in the central region ($R < 350$ kpc), which is the one of interest in the following strong-lensing analysis, is remarkably good.

3. Strong-lensing Analysis

As done in Ca17, we combine the exquisite quality of the HFF images (Lotz et al. 2017) with the power of the MUSE integral-field spectrograph (Bacon et al. 2012) to reconstruct the total mass distribution of MACS 0416. Due to the small differences with the work of Ca17, namely, the separate treatment of two member galaxies (see Section 3.1), we decided to rerun the reference model (hereafter REF). The new model (hereafter GAS) presented in this work is the same as REF, but with the hot gas included as a separate fixed mass component.

We briefly describe the multiple image and member galaxy catalogs we use in this analysis; for more details we refer the reader to Ca17. The multiple-image catalog contains 102 images from 37 systems spanning a range in redshift from $z \approx 0.94$ to $z \approx 6.15$ and consists only of systems with secure identification (Balestra et al. 2016; Caminha et al. 2016) and spectroscopic redshift. The 193 member galaxies have been selected on the basis of the available photometric *HST* and spectroscopic VLT data; in detail, 144 galaxies have a spectroscopic redshift measurement, while the remaining ones have been chosen based on their n-dimensional distance, in color space, from the locus of the spectroscopically confirmed member galaxies (for more details, see Gr15).

The redshifts have been estimated from two sets of archival MUSE observations of the northeast (program ID 094.A-0115B, PI: J. Richard) and southwest (program ID 094.A-0525(A), PI: F. E. Bauer) regions.

3.1. Lens Mass Modeling

We distinguish the different mass components of the cluster into three main families: diffuse main halos (mainly dark matter plus a few percent intracluster light), member galaxies (with their respective dark matter halos), and hot gas (as discussed in Section 2).

All components are described by dPIE profiles (see Equation (2)), for which the convergence is

$$\kappa(x, y) = \frac{\sigma_0^2 R_T}{2G\Sigma_{\rm cr}(R_T - R_C)}\left(\frac{1}{\sqrt{R_C^2 + R^2}} - \frac{1}{\sqrt{R_T^2 + R^2}}\right), \quad (10)$$

where σ_0 is the central velocity dispersion, R_C is the core radius, R_T is the truncation radius, $\Sigma_{\rm cr}$ is the critical surface density, and R is the radial distance from the mass center. Including a possible elongation term on the plane of the sky, the definition of R becomes $R^2 = x^2(1+\epsilon)^{-2} + y^2(1-\epsilon)^{-2}$, with the ellipticity ϵ defined as $\epsilon \equiv (1-q)/(1+q)$ and q being the minor-to-major-axis ratio.

Given the complex structure of MACS 0416, visible for example in its luminosity distribution, we adopt two dPIE components for the diffuse halos. We fix their truncation radii to infinity, effectively making them equivalent to pseudo-isothermal elliptical mass distribution (hereafter PIEMD; Kassiola & Kovner 1993) profiles. Each of these two components has six free parameters: the center coordinates, x_h and y_h, the ellipticity and position angle, ϵ_h and θ_h, the core radius, $R_{C,h}$, and the central velocity dispersion, $\sigma_{0,h}$. As explained in Ca17, the addition of a third diffuse halo is required to reduce the offset between the positions of observed and model-predicted multiple images in the northeast region of the northern BCG, G1. This halo is assumed to be spherical; therefore, it is described by only four parameters: x_{h3}, y_{h3}, $R_{C,h3}$, and $\sigma_{0,h3}$.

Each member galaxy is modeled with a spherical dPIE profile with vanishing core radius and center fixed at the position of the galaxy luminosity center. To reduce the number of free parameters, we scale the values of $\sigma_{0,i}$ and $R_{T,i}$ of each galaxy depending on its luminosity L_i (in the *HST*/WFC3 filter F160W). We refer to these values as $\sigma_{0,g}$ and $R_{T,g}$, the velocity dispersion and truncation radius of the reference galaxy, G1, with luminosity L_g ($\rm mag_{F160W} = 17.02$),

$$\sigma_{0,i} = \sigma_{0,g}\left(\frac{L_i}{L_g}\right)^{0.35} \quad \text{and} \quad R_{T,i} = R_{T,g}\left(\frac{L_i}{L_g}\right)^{0.5}. \quad (11)$$

These scaling relations have been chosen as they reproduce the tilt of the fundamental plane (Faber et al. 1987; Bender et al. 1992) observed in early-type galaxies. Additionally, they have been shown to describe accurately the total mass properties of member

galaxies in MACS 0416 (Gr15, Ca17), MACS J1149.5+2223 (Grillo et al. 2016), and RXC J2248.7–4431 (Caminha et al. 2016). We do not treat separately the two member galaxies mainly responsible for the appearance of the multiple images of family 14, contrary to what has been done by Ca17. We model these two galaxies using the same scaling relations adopted for the other member galaxies.

We include an additional galaxy halo at the location of a foreground galaxy in the southwest region of the cluster (R.A. = 04:16:06.82, decl. = –24:05:08.4). Given that this galaxy does not belong to the cluster ($z = 0.112$), its σ_0 and R_T should be considered only as effective parameters.

In the GAS model, we include a component for the hot gas distribution, as derived from the analysis of the X-ray surface brightness presented in Section 2. We keep this component fixed, when fitting the multiple image positions. The inclusion as a fixed component is justified by the smaller set of assumptions required to derive the gas density profile from the X-ray surface brightness. Besides, the statistical errors on the hot gas mass profile are smaller than those typically associated with the other cluster mass components.

We use the software *lenstool* (Jullo et al. 2007) to infer the best-fitting values of the parameters of the total mass models of MACS 0416, using the positions of multiple images as observables. Furthermore, we adopt uniform priors for all model parameters.

In summary, we use two descriptions for the cluster total mass: a reference model (REF), where the diffuse component includes the hot gas, and the new one (GAS), where the hot gas distribution is fixed to the result of an X-ray surface brightness analysis. Both of them have the same number of free parameters, as the separate hot gas mass density is not optimized in the lensing modeling.

For each model, we initially adopt an error on the position of the multiple images of 0.″5, the same value as in Ca17 and close to the theoretical prediction by Jullo et al. (2010). The resulting best-fitting models have a reduced χ^2 larger than unity (1.2 and 1.3 for REF and GAS, respectively). In order to get realistic uncertainties for the model parameters, the χ^2 should be comparable with the number of degrees of freedom (110). Therefore, we rerun the MCMC analysis using an image positional error of 0.″58. This value has been obtained by requiring that the reduced χ^2 of the best-fitting models is approximately 1. By increasing the uncertainty of the image positions, we take into account unknown factors, such as line-of-sight mass structures or small dark matter clumps in the cluster, which affect the observed positions of the images. Hereafter, we will refer only to the second runs, with 0.″58 positional errors, when presenting the results. We run the MCMC analysis until convergence, resulting in a total of more than 1.1×10^5 points that sample the posterior probability distribution of the model parameters.

4. Results

In this section, we present the results of the two mass models we have obtained for MACS 0416, namely, the reference model (REF) and the model where the hot gas component has been included separately (GAS).

The values of the parameters inferred for the two models are shown in Table 3, where we quote the median values and the 68%, 95%, and 99.7% confidence level (CL) intervals. The positions of the centers are given relatively to the northern BCG, G1. The best-fit χ^2 values (logarithmic Bayesian evidence) are 99.5 (−202.3) and 105.5 (−201.3) for the REF and GAS model, respectively, corresponding to rms values of 0.″57 and 0.″59 (median values 0.″40 and 0.″41) for the offset between the observed and model-predicted positions of the multiple images. Given that both models have the same number of degrees of freedom (110), it is remarkable that we obtain similar χ^2 values when we fix some percent (about 10%, as estimated below) of the cluster total mass in the hot gas component.

In the case of the Bullet cluster, Paraficz et al. (2016) found that the model with a separate hot gas component is strongly preferred, mostly due to the large offset between the gas and dark matter components. Our new approach allows us to more accurately characterize the collisional and collisionless components, even in less extreme merging conditions.

For the GAS model, we show the posterior probability distributions of the parameters of the three main halos (see Appendix A) and of the member galaxy scaling relations (see Figure 3). Here the blue contours contain 39.3%, 86.5%, and 98.9% of the samples, which correspond to the 1σ, 2σ, and 3σ of a 2D Gaussian distribution; the black solid lines are the median values of the reference model. In the 1D histograms, vertical blue dashed lines coincide with 16th, 50th, and 84th percentiles. Out of the correlation plots not shown here, there are no strong degeneracies among different halo parameters. Only weak correlations are visible between the parameters of the northeast and third halos, which are to be expected given their close distance in projection.

Interestingly, the MCMC chains converge to values that are very similar to those presented in Ca17, with the exception of $R_{T,g}$ and $\sigma_{0,g}$; however, these are still consistent within 1σ uncertainties. While our reference model seems to favor more compact member galaxies with higher central velocity dispersions, Ca17 found a median value of $\sigma_{0,g}$ that corresponds with the secondary peak ($\sigma_{0,g} \approx 240\,\mathrm{km\,s^{-1}}$) in our marginalized distribution shown in Figure 3.

The inclusion of a separate hot gas component does not change substantially the inferred properties of the diffuse halo components (all the values of their parameters are within 3σ with respect to those of the reference model). As expected, the velocity dispersion and core radius values of the diffuse halos change the most, as these parameters are proportional to the square root of the mass of the corresponding component. This follows from the fact that the gas mass is now modeled separately and not included in the diffuse halos, as in the reference model.

We estimate the cumulative projected mass profile of the various components: total, diffuse halos (mostly dark matter), member galaxies, and hot gas. These are shown, respectively, in black, blue, green, and red in the top and middle panels of Figure 4. A subsample of the MCMC chains is shown as thin lines, and their median and 16th–84th percentiles are shown with solid and dashed lines. The top panel corresponds to the REF model, while the middle one corresponds to the GAS model. Noticeably, the total and member galaxy mass profiles are very similar in the two models. This agreement confirms the above statement that the hot gas mass component is essentially subtracted from that of the main halos, not affecting the total or the member galaxy mass estimates. The decrease of mass in the diffuse halos is more evident in the bottom panel of Figure 4,

Table 3
Values of the Parameters of the Lens Models of MACS 0416

Parameter	REF Median	REF 68% CL	REF 95% CL	REF 99.7% CL	GAS Median	GAS 68% CL	GAS 95% CL	GAS 99.7% CL	
x_{h1} ($''$)	−2.0	$^{+1.0}_{-1.0}$	$^{+1.8}_{-1.7}$	$^{+2.8}_{-2.3}$	−2.4	$^{+1.0}_{-0.8}$	$^{+2.3}_{-1.5}$	$^{+3.4}_{-2.2}$	x_{h1} ($''$)
y_{h1} ($''$)	1.4	$^{+0.7}_{-0.7}$	$^{+1.2}_{-1.5}$	$^{+1.6}_{-2.2}$	1.7	$^{+0.5}_{-0.7}$	$^{+0.9}_{-1.7}$	$^{+1.3}_{-2.7}$	y_{h1} ($''$)
ϵ_{h1}	0.84	$^{+0.02}_{-0.06}$	$^{+0.04}_{-0.11}$	$^{+0.05}_{-0.14}$	0.85	$^{+0.02}_{-0.02}$	$^{+0.03}_{-0.08}$	$^{+0.04}_{-0.12}$	ϵ_{h1}
θ_{h1} (degree)	144.7	$^{+1.2}_{-1.1}$	$^{+2.8}_{-2.5}$	$^{+4.2}_{-4.3}$	145.1	$^{+0.9}_{-0.9}$	$^{+2.1}_{-2.0}$	$^{+3.9}_{-3.6}$	θ_{h1} (degree)
$R_{C,h1}$ ($''$)	6.7	$^{+0.9}_{-0.9}$	$^{+1.7}_{-1.8}$	$^{+2.5}_{-2.8}$	6.8	$^{+0.8}_{-1.0}$	$^{+1.5}_{-1.9}$	$^{+2.4}_{-2.7}$	$R_{C,h1}$ ($''$)
$\sigma_{0,h1}$ (km s^{-1})	713	$^{+32}_{-34}$	$^{+60}_{-70}$	$^{+90}_{-120}$	708	$^{+26}_{-29}$	$^{+48}_{-67}$	$^{+71}_{-102}$	$\sigma_{0,h1}$ (km s^{-1})
x_{h2} ($''$)	20.1	$^{+0.4}_{-0.5}$	$^{+1.1}_{-1.0}$	$^{+1.7}_{-1.4}$	20.0	$^{+0.4}_{-0.4}$	$^{+0.9}_{-0.9}$	$^{+1.6}_{-1.3}$	x_{h2} ($''$)
y_{h2} ($''$)	−37.1	$^{+0.8}_{-0.8}$	$^{+1.6}_{-1.7}$	$^{+2.3}_{-2.7}$	−37.0	$^{+0.7}_{-0.7}$	$^{+1.5}_{-1.5}$	$^{+2.1}_{-2.6}$	y_{h2} ($''$)
ϵ_{h2}	0.76	$^{+0.02}_{-0.02}$	$^{+0.03}_{-0.03}$	$^{+0.05}_{-0.07}$	0.77	$^{+0.02}_{-0.01}$	$^{+0.03}_{-0.03}$	$^{+0.04}_{-0.05}$	ϵ_{h2}
θ_{h2} (degree)	125.8	$^{+0.5}_{-0.5}$	$^{+1.0}_{-1.0}$	$^{+1.6}_{-1.5}$	125.9	$^{+0.4}_{-0.4}$	$^{+0.9}_{-0.8}$	$^{+1.4}_{-1.3}$	θ_{h2} (degree)
$R_{C,h2}$ ($''$)	13.2	$^{+0.9}_{-0.9}$	$^{+1.7}_{-1.6}$	$^{+2.5}_{-2.3}$	12.6	$^{+0.7}_{-0.7}$	$^{+1.4}_{-1.4}$	$^{+2.2}_{-2.2}$	$R_{C,h2}$ ($''$)
$\sigma_{0,h2}$ (km s^{-1})	1103	$^{+22}_{-22}$	$^{+43}_{-45}$	$^{+73}_{-81}$	1065	$^{+19}_{-20}$	$^{+39}_{-38}$	$^{+62}_{-60}$	$\sigma_{0,h2}$ (km s^{-1})
x_{h3} ($''$)	−34.3	$^{+1.2}_{-1.5}$	$^{+2.2}_{-3.7}$	$^{+3.4}_{-6.8}$	−34.3	$^{+1.0}_{-1.3}$	$^{+2.0}_{-3.4}$	$^{+3.1}_{-5.8}$	x_{h3} ($''$)
y_{h3} ($''$)	8.7	$^{+3.3}_{-1.3}$	$^{+4.9}_{-2.0}$	$^{+6.9}_{-2.8}$	8.1	$^{+1.6}_{-0.8}$	$^{+5.0}_{-1.4}$	$^{+6.8}_{-2.1}$	y_{h3} ($''$)
$R_{C,h3}$ ($''$)	7.5	$^{+2.4}_{-2.7}$	$^{+4.9}_{-5.2}$	$^{+8.0}_{-7.1}$	4.6	$^{+3.0}_{-2.4}$	$^{+5.5}_{-4.0}$	$^{+7.9}_{-4.5}$	$R_{C,h3}$ ($''$)
$\sigma_{0,h3}$ (km s^{-1})	435	$^{+59}_{-62}$	$^{+125}_{-117}$	$^{+192}_{-156}$	351	$^{+64}_{-51}$	$^{+131}_{-87}$	$^{+191}_{-112}$	$\sigma_{0,h3}$ (km s^{-1})
$R_{T,g}$ ($''$)	7.8	$^{+4.3}_{-2.4}$	$^{+11.9}_{-3.5}$	$^{+37.0}_{-4.3}$	7.7	$^{+3.6}_{-2.0}$	$^{+10.5}_{-3.7}$	$^{+14.9}_{-4.5}$	$R_{T,g}$ ($''$)
$\sigma_{0,g}$ (km s^{-1})	321	$^{+27}_{-77}$	$^{+46}_{-102}$	$^{+61}_{-136}$	317	$^{+17}_{-72}$	$^{+44}_{-103}$	$^{+62}_{-128}$	$\sigma_{0,g}$ (km s^{-1})

Note. Median values and confidence level (CL) uncertainties are given for the two models presented in the paper. Centers are relative to the northeast BCG, G1 (R. A. = 04:16:09.154, decl. = –24:04:02.90). The angles θ_{h1} and θ_{h2} are measured counterclockwise from the west axis.

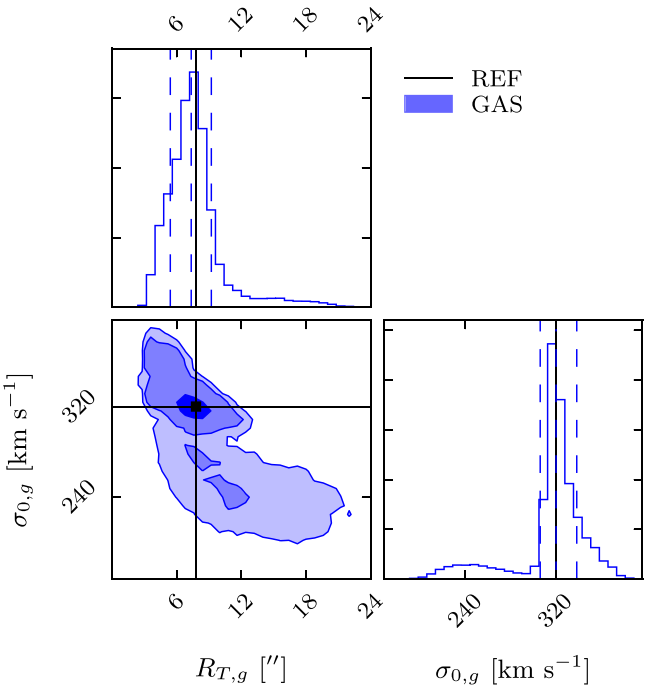

Figure 3. Posterior distributions of the values of the northeast BCG (G1) parameters (entering in Equation (10)) derived from the lensing model with the hot gas component included separately (i.e., GAS model). Blue contours contain 39.3%, 86.5%, and 98.9% of the samples, while blue dashed lines in the 1D histograms show the 16th, 50th, and 84th percentiles. Black solid lines mark the median values of the reference model (i.e., REF model).

where the relative difference in enclosed mass between the two models is shown for the total mass (black) and the diffuse halos (blue). This plot simply shows the ratios of the two black and two blue curves of the panels above. We exclude from the figure a comparison of the member galaxy component, as the error in the mass ratio is too large to give any useful information. As noted before, the total mass measurements of the two models are consistent within the errors, while the mass in the diffuse halo component decreases, once the hot gas is treated separately. This difference is significant at more than 3σ above 100 kpc, and we find approximately 10% less mass (at a radial distance of approximately 350 kpc from the main BCG) in the diffuse halos in our refined model.

Interestingly, looking at the middle panel of Figure 4, the mass in the diffuse halo component is almost a constant fraction of the total mass, outside the region where the BCG contribution might still be very relevant ($R > 40$ kpc). To better quantify this feature, in Figure 5 we plot the cumulative projected diffuse halo over total mass profile for the REF (black) and GAS (red) models. The central solid lines mark the median values, and the colored regions show the 1σ, 2σ, and 3σ confidence regions, similarly to the previous plot. Having removed the hot gas component from the diffuse halos, the red profile describes more realistically than the black one the cluster dark matter over total mass fraction. Moving toward the center of the cluster, the fraction of dark matter varies slowly and begins to decrease noticeably only around the BCG truncation radius $R_{T,g} \approx 40$ kpc (marked with a vertical dashed line).

Moreover, we provide maps of the total and gas surface mass densities (left panel of Figure 6), derived from our refined best-fitting model GAS, which we then use to obtain a map of the local gas-to-total mass fraction (right panel). The white curves, overlaid on top of the HFF color image, are isodensity contours of the total mass, from 3.5×10^8 to $2.85 \times 10^9\ M_\odot/\mathrm{kpc}^2$, with a linear step of $2.5 \times 10^8\ M_\odot/\mathrm{kpc}^2$; the red ones show the hot gas component, from 4.5×10^7 to $1.35 \times 10^8\ M_\odot/\mathrm{kpc}^2$, with a

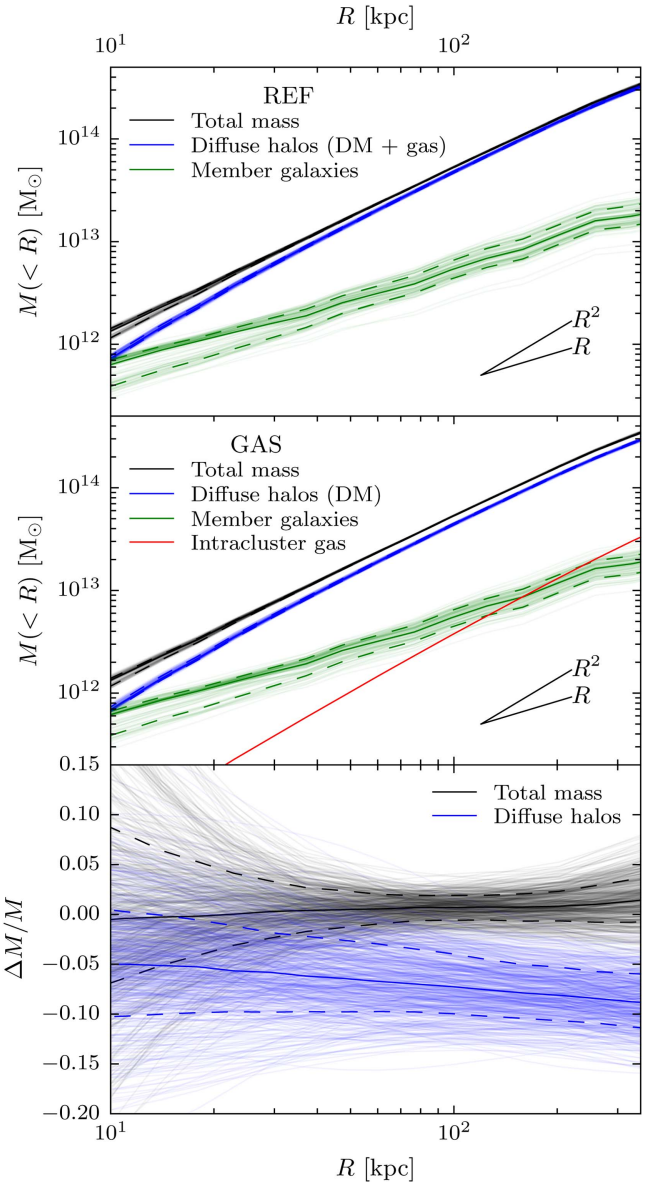

Figure 4. Radial profiles of cumulative projected mass of MACS 0416 for the reference (top panel) and separate gas (middle panel) models. Black, blue, green, and red curves represent the total, diffuse halos, galaxy members, and hot intracluster gas profiles, respectively. Thin lines show a subsample of the models in the final MCMC chains, while solid and dashed lines give the median and 16th–84th percentiles. We indicate the values of the central logarithmic slope corresponding to a cored and a singular isothermal sphere surface mass distribution, 2 and 1, respectively. The bottom panel shows the relative difference between the same components of the two models: in black the total and in blue the diffuse halo mass.

linear step of $1.5 \times 10^7\ M_\odot/\mathrm{kpc}^2$. The blue and red plus signs mark the location of the maximum values in the dark matter and intracluster hot gas surface mass density maps. The filled contours shown in the right panel trace the gas-to-total mass fraction computed from the maps of the gas and total surface mass densities. The white circles locate the positions of the member galaxies, and the circle area is proportional to the *H*-band luminosity of the galaxy they represent. We mask (in gray) the outer regions of the cluster, where there is no lensing information from observed multiple images, thus making the

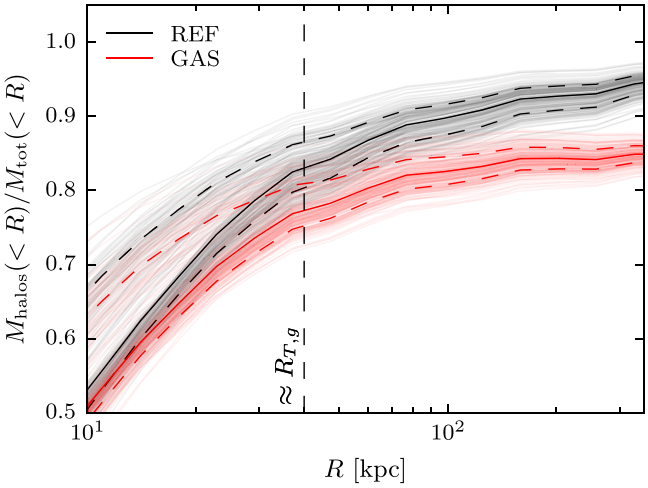

Figure 5. Radial profiles of the fraction of cumulative projected total mass in the diffuse halo component (mostly dark matter). Black curves show the halos that include both the dark matter and hot intracluster gas components (i.e., REF model), while the red curves represent the dark-matter-only component (i.e., GAS model). Thin lines show a subsample of the models in the final MCMC chains, while solid and dashed lines give the median and 16th–84th percentiles, respectively. The vertical dashed line shows approximately the truncation radius of the BCG G1.

cluster mass reconstruction here less accurate. One of the reasons for the separate inclusion of the hot gas component in cluster lensing analyses is evident from these two plots: dark matter and intracluster gas are distributed slightly differently, the former appearing more elongated than the latter.

For the two main subclusters, we have computed the distance between the density peaks of each component and the closest BCG. In the northeast sector, these correspond to approximately 2″ (peak located at R.A. = 4:16:09.276, decl. = –24:04:01.87) and 3″ (peak located at R.A. = 4:16:09.373, decl. = –24:04:02.73) for the dark matter and hot intracluster gas densities, respectively. In the southwest subcluster, the densities of the two components peak at distances of approximately 1″ (peak located at R.A. = 4:16:07.718, decl. = –24:04:39.04) and 6″ (peak located at R.A. = 4:16:07.497, decl. = –24:04:44.49). Given statistical and systematic uncertainties of a few arcseconds in the position of the peaks, the only evidence for an offset is for the gas component in the southwest (about 2σ–3σ). This offset is smaller than the one found in Jauzac et al. (2015), and the position of the hot gas density peak is consistent with the uncertainty region in the X-ray surface brightness peak presented in Ogrean et al. (2015); we refer to Gr15 and Balestra et al. (2016) for further details.

A difference in the centers of the dark matter and hot gas mass distributions is another effect traditionally not included in strong-lensing models. As mentioned previously (see Section 1 and Markevitch et al. 2004), it is in principle possible to determine the cross section of SIDM from the offset between the member galaxy and dark matter distributions; therefore, it is extremely important to have an accurate measurement of the center of the dark matter component, without the bias introduced by the intracluster gas, which lags behind in merging events owing to its collisional behavior.

Naturally, possible differences between the distributions of dark matter and hot gas are reflected into the gas-to-total mass

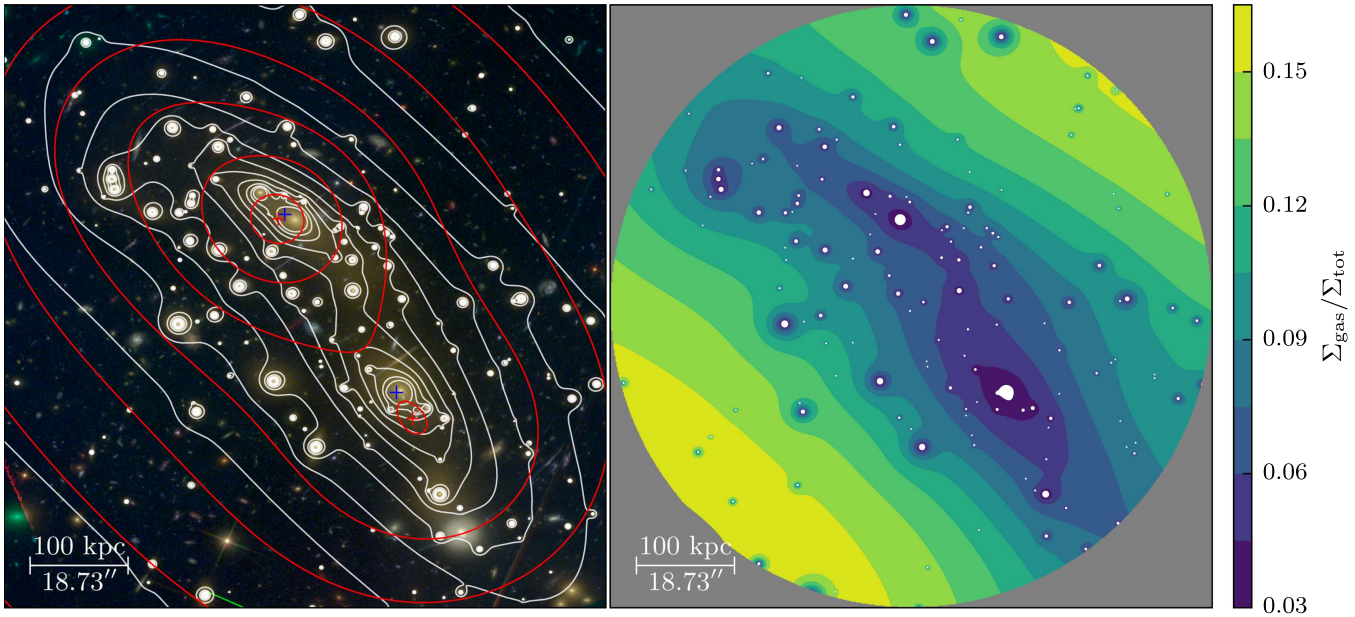

Figure 6. Left: total (white) and hot gas (red) surface mass density isocontours overlaid on a color-composite *HST* WCF3+ACS image of MACS 0416 (seven filters from the Hubble Frontier Fields data; see Caminha et al. 2017). Total mass isodensities have a linear step of $2.5 \times 10^8\,M_\odot\,\mathrm{kpc}^{-2}$ and go from 3.5×10^8 to $2.85 \times 10^9\,M_\odot\,\mathrm{kpc}^{-2}$. Hot gas isodensities go from 4.5×10^7 to $1.35 \times 10^8\,M_\odot\,\mathrm{kpc}^{-2}$ with a linear step of $1.5 \times 10^7\,M_\odot\,\mathrm{kpc}^{-2}$. The peaks of the surface mass density maps are shown with blue and red plus signs, for the diffuse dark matter and intracluster hot gas, respectively. Right: local gas-to-total mass fraction map, derived from the surface mass density maps. White circles show the member galaxies, with each circle area proportional to the galaxy luminosity.

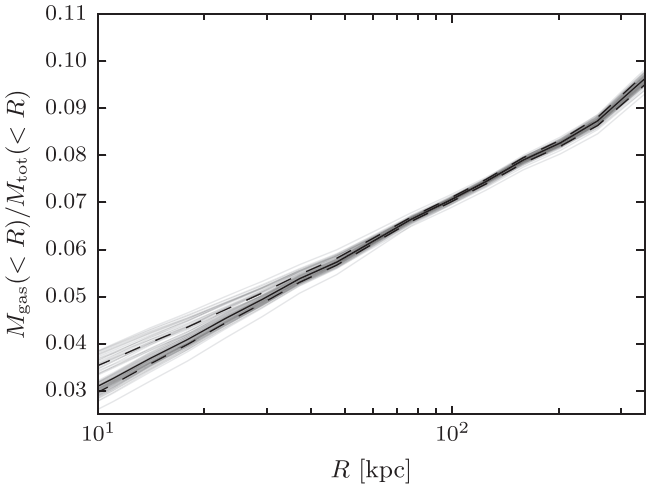

Figure 7. Cumulative projected gas-to-total mass fraction computed from the cumulative 2D mass profiles. Thin lines show a subsample of the MCMC models, while solid and dashed lines give the median and 16th–84th percentiles, respectively.

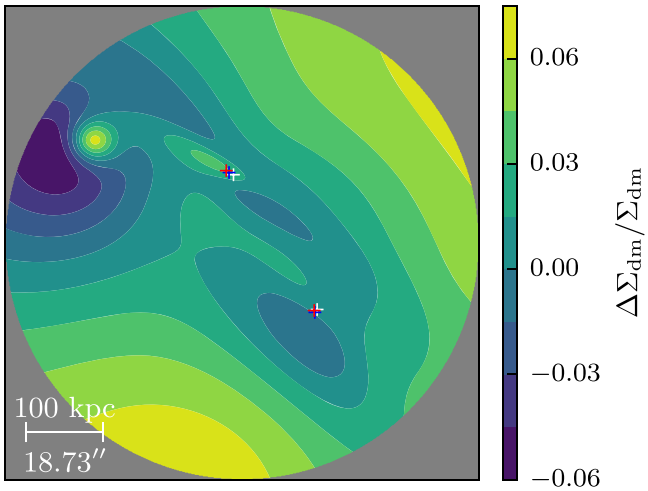

Figure 8. Relative difference between the proposed method and an a posteriori analysis in the diffuse dark matter surface mass density. Plus signs mark the BCGs (white) and the peaks of the diffuse dark matter distribution of the GAS (red) and POST (blue) models, respectively.

fraction map. For instance, the larger core of the hot gas mass component creates two peaks in the map at the location of the two BCGs.

Finally, we compute the cumulative projected gas-to-total mass fraction as a function of the distance from G1, shown in Figure 7. As in Figure 4, solid and dashed lines show the median and 16th–84th percentiles, while the thin lines are obtained from a subsample of the models extracted from the MCMC chain. As we assume a fixed gas profile, the errors shown here underestimate the true uncertainties in the gas fraction. Clearly, gravitational lensing can only provide 2D information about the total mass of a lens, and a deprojection of the mass distribution in a merging cluster, like MACS 0416, is not a trivial task. This would require several assumptions about the symmetry of the system. Hence, we decide to use our 2D mass densities in the computation of the gas fraction. The projected gas-to-total mass fraction within an aperture of 350 kpc is approximately 10%. A direct

comparison with the results by Jauzac et al. (2015) is not possible because the (de)projection method used to compute the gas-to-total mass fraction, shown in their Figure 11, is not fully described.

In passing, we mention that we have also subtracted the hot gas surface mass density reconstructed in Section 2 from the diffuse halo surface mass density of the best-fit REF model, to mimic the results one would obtain in a posteriori analyses. Figure 8 shows the relative difference between the best-fit models of the proposed method (GAS) and an a posteriori analysis (POST) in the estimate of the diffuse dark matter-only surface mass density. The white plus signs show the position of the BCGs, G1 and G2, and the peaks of the diffuse dark matter distribution of the GAS and POST models are marked with red and blue plus signs, respectively. The differences in the dark matter surface mass density are quite noticeable in the northeast region, around the third halo, but are overall small (less than 6%). Similarly, the position of the peak of the northeast component changes slightly, resulting in a difference of approximately $1''$ between the GAS and POST models. Although the dark matter surface mass density maps of the two approaches in MACS 0416 are very similar, the advantage of the method we adopt in this work is the direct measurement of the parameter values of the dark matter-only distribution, unavailable in a traditional analysis.

5. Conclusions

In this paper, we have presented a novel approach to include the hot gas component in strong gravitational lensing analyses. The method starts from a separate modeling of the X-ray surface brightness to derive the distribution of the intracluster gas, which is then used as an additional fixed mass component to the lensing fit. By doing so, we can disentangle the cluster hot gas from the diffuse main halo, thus tracing more accurately the noncollisional mass component, i.e., mainly dark matter. We have applied this method to the HFF merging cluster MACS J0416.1–2403, which was the target of several recent spectroscopic campaigns (Grillo et al. 2015; Balestra et al. 2016; Hoag et al. 2016; Caminha et al. 2017). We have fitted the observed positions of a large set of spectroscopically confirmed multiple images with two lensing models: one adopting our new technique (GAS) and one following a traditional modeling of the intracluster gas included in the main diffuse halos (REF).

The main results of the work can be summarized as follows:

1. We have provided an analytical solution for the X-ray surface brightness emission produced by multiple dPIE mass density distributions. This profile is commonly used in the lensing community and therefore readily available "out of the box" in most gravitational lensing softwares, as opposed to the β-model profile, widely adopted in X-ray analyses.
2. Using the aforementioned profile, we have fitted deep *Chandra* observations of the X-ray surface brightness of MACS 0416. We have found a best-fitting model consisting of two diffuse components with similar values of $R_C \approx 180$ kpc for the core radius. An additional, more compact, dPIE distribution is required to match the peaked emission in the central regions of the northeast clump. Our findings are in agreement with those of a previous work by Ogrean et al. (2015) and with the results of a radial deprojection technique.
3. Once the intracluster gas is included as a separate mass component, the values of the parameters inferred from the new lensing analysis are similar to those obtained in the reference model (in all cases within the 3σ confidence levels, given the current model and data uncertainties). Moreover, the total mass does not change between the two models and only the diffuse halo contribution is reduced, by approximately 10%, while the mass of the member galaxies remains the same.
4. Taking advantage of our new model, we have reconstructed the spatial distribution of the total and intracluster gas surface mass density of MACS 0416, showing some spatial differences between the collisional and noncollisional matter. This provides a more self-consistent measurement of these two, intrinsically different, mass components. The measured offset, of about $6''$ in the southwest region, is consistent with MACS 0416 being in the initial phase of pre-merging, as discussed in Balestra et al. (2016), with the gas components mildly trailing behind the noncollisional components (stars and dark matter). Furthermore, our method provides a possibly unbiased measurement of the center of the dark matter distribution, a quantity that can be used to measure the cross section of SIDM.
5. We have found that in MACS 0416 the projected fraction of total mass in diffuse halos, composed mainly of dark matter, is almost constant in the region from $\approx$70 kpc out to more than 350 kpc from the northern BCG. This demonstrates the importance of modeling separately and disentangling the hot gas component to measure more accurately the dark matter distribution in galaxy clusters.
6. Finally, we have provided both the 2D map and the 1D cumulative profile of the projected gas-to-total mass fraction. From our model of the X-ray surface brightness, we have estimated that the projected gas mass within an aperture of 350 kpc is $M_{\rm gas}(R < 350\ {\rm kpc}) = 3.3 \times 10^{13}\, M_{\odot}$ (with a few percent statistical errors), which gives a projected gas fraction of approximately 10%.

The framework we have presented combines X-ray and lensing observables in a more consistent way than a posteriori analyses: this is a step forward in a broader effort to paint a multiwavelength picture of clusters of galaxies, complementary to the other joint techniques. In MACS 0416, a simpler analysis, where the hot gas is subtracted from the diffuse halo, results in a similar cumulative mass profile for the dark matter component. Despite that, we have shown that our improved mass model can determine more accurately the values of the parameters adopted to describe the inner dark matter distribution of a cluster, thus providing more suitable results to test different structure formation scenarios and the collision-less nature of dark matter.

M.B. and C.G. acknowledge support by the VILLUM FONDEN Young Investigator Programme through grant no. 10123. S.E. acknowledges the financial support from contracts ASI-INAF I/009/10/0, and ASI 2015-046-R.0. G.B.C., P.R., A.M., M.A., and M.L. acknowledge financial support from PRIN-INAF 2014 1.05.01.94.02. Corner plots were created using the *corner.py* module (Foreman-Mackey 2016).

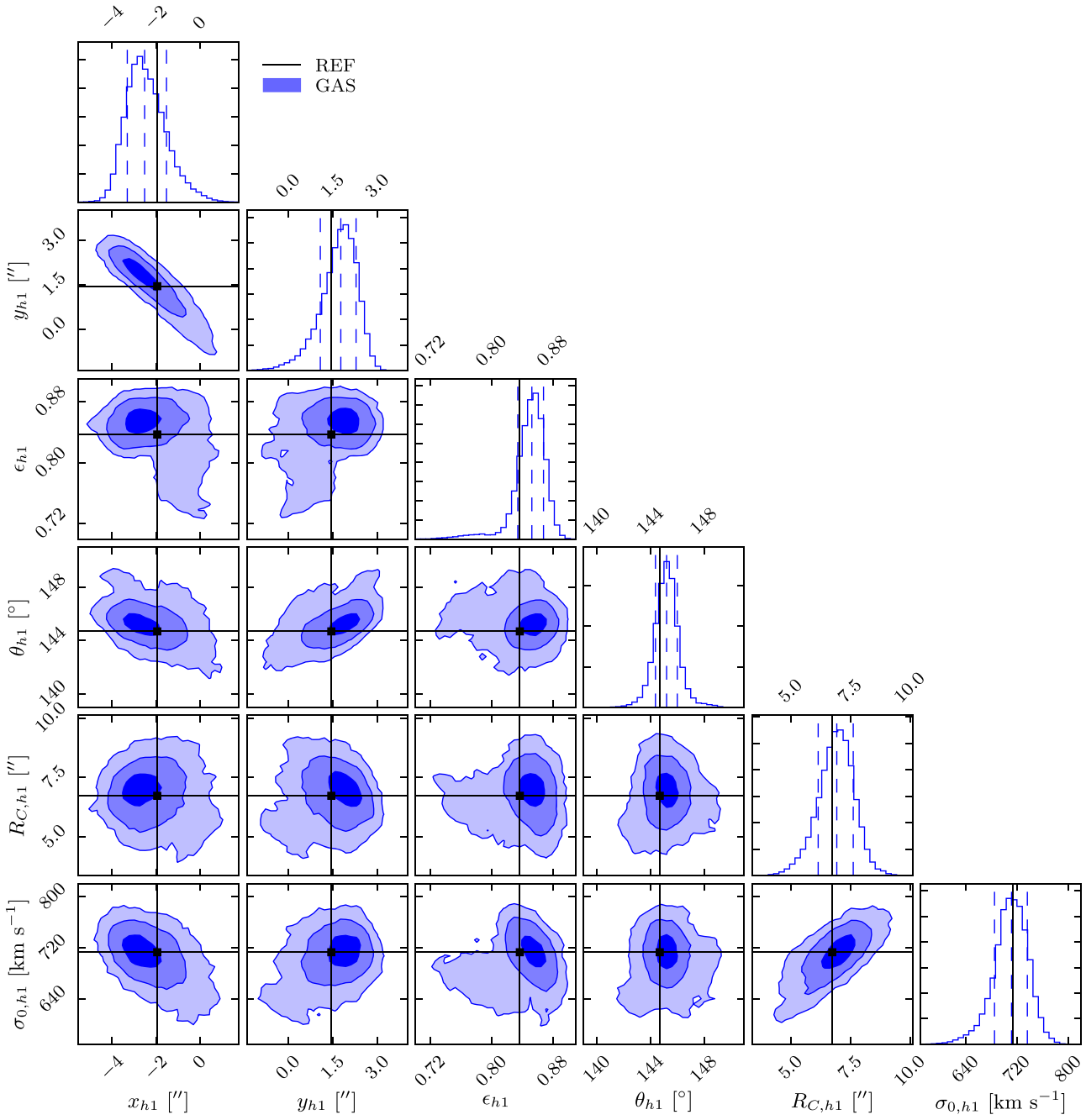

Figure 9. Posterior distributions of the values of the northeast main halo parameters derived from the strong-lensing model with the hot gas included separately (i.e., GAS model). Blue contours contain 39.3%, 86.5%, and 98.9% of the samples, while blue dashed lines in the 1D histograms show the 16th, 50th, and 84th percentiles. Black solid lines mark the median values of the reference model (i.e., REF model).

Appendix A
Posterior Distributions

Hereafter (Figures 9–11) we show the posterior distributions of the parameter values of the main halos of MACS 0416 derived from the strong-lensing model with the hot gas included separately (i.e., GAS model). As described above, blue contours contains the 39.3%, 86.5%, and 98.9% of the samples, which correspond to the 1σ, 2σ, and 3σ of a 2D Gaussian distribution, while the black solid lines are the median values from the reference model (i.e., REF model). In the 1D histograms, vertical blue dashed lines coincide with 16th, 50th, and 84th percentiles.

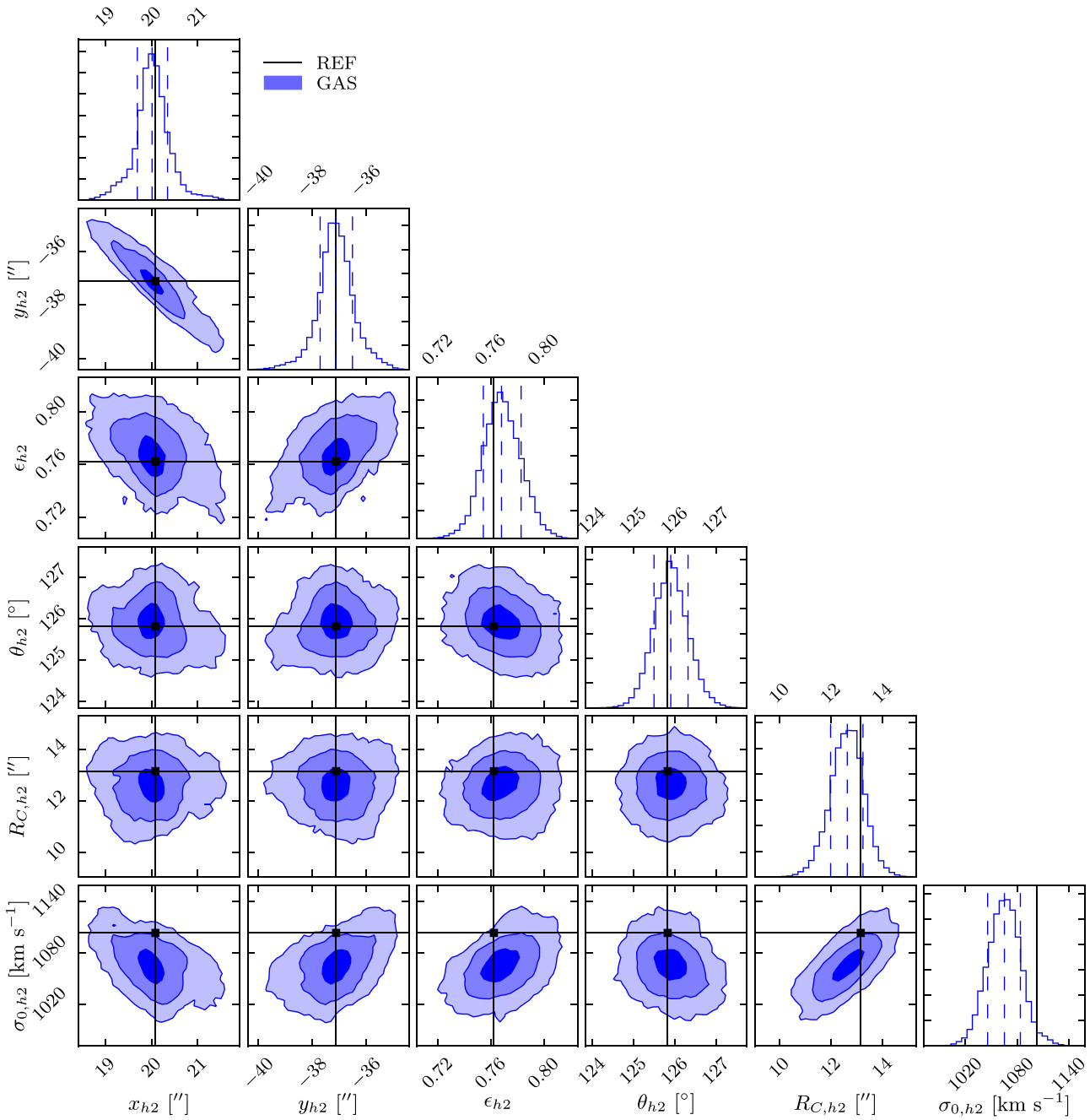

Figure 10. Posterior distributions of the values of the southwest main halo parameters derived from the strong-lensing model with the hot gas included separately (i.e., GAS model). Blue contours contain 39.3%, 86.5%, and 98.9% of the samples, while blue dashed lines in the 1D histograms show the 16th, 50th, and 84th percentiles. Black solid lines mark the median values of the reference model (i.e., REF model).

Appendix B
Analytical Solution for Two-component Spherical and Ellipsoidal dPIE Models

We can use the analytical solution presented in Equation (6) to obtain explicitly the X-ray surface brightness of a system consisting of two dPIE components:

$$S_X(x,y) \propto \int_{-\infty}^{+\infty} \rho^2 dz = \frac{\pi\rho_{01}^2 R_{C1}^4 R_{T1}^4 (R_{A1}^2 + 3R_{A1}R_{B1} + R_{B1}^2)}{2R_{A1}^3 R_{B1}^3 (R_{A1}+R_{B1})^3} + \frac{\pi\rho_{02}^2 R_{C2}^4 R_{T2}^4 (R_{A2}^2 + 3R_{A2}R_{B2} + R_{B2}^2)}{2R_{A2}^3 R_{B2}^3 (R_{A2}+R_{B2})^3}$$
$$+ 2\pi(\rho_{01}R_{C1}^2 R_{T1}^2)(\rho_{02}R_{C2}^2 R_{T2}^2) \frac{R_{A1}^2(R_{B1}+R_{A2}+R_{B2}) + R_{A1}(R_{B1}+R_{A2}+R_{B2})^2 + (R_{B1}+R_{A2})(R_{B1}+R_{B2})(R_{A2}+R_{B2})}{R_{A1}R_{B1}R_{A2}R_{B2}(R_{A1}+R_{B1})(R_{A1}+R_{A2})(R_{A1}+R_{B2})(R_{B1}+R_{A2})(R_{B1}+R_{B2})(R_{A2}+R_{B2})}. \quad (12)$$

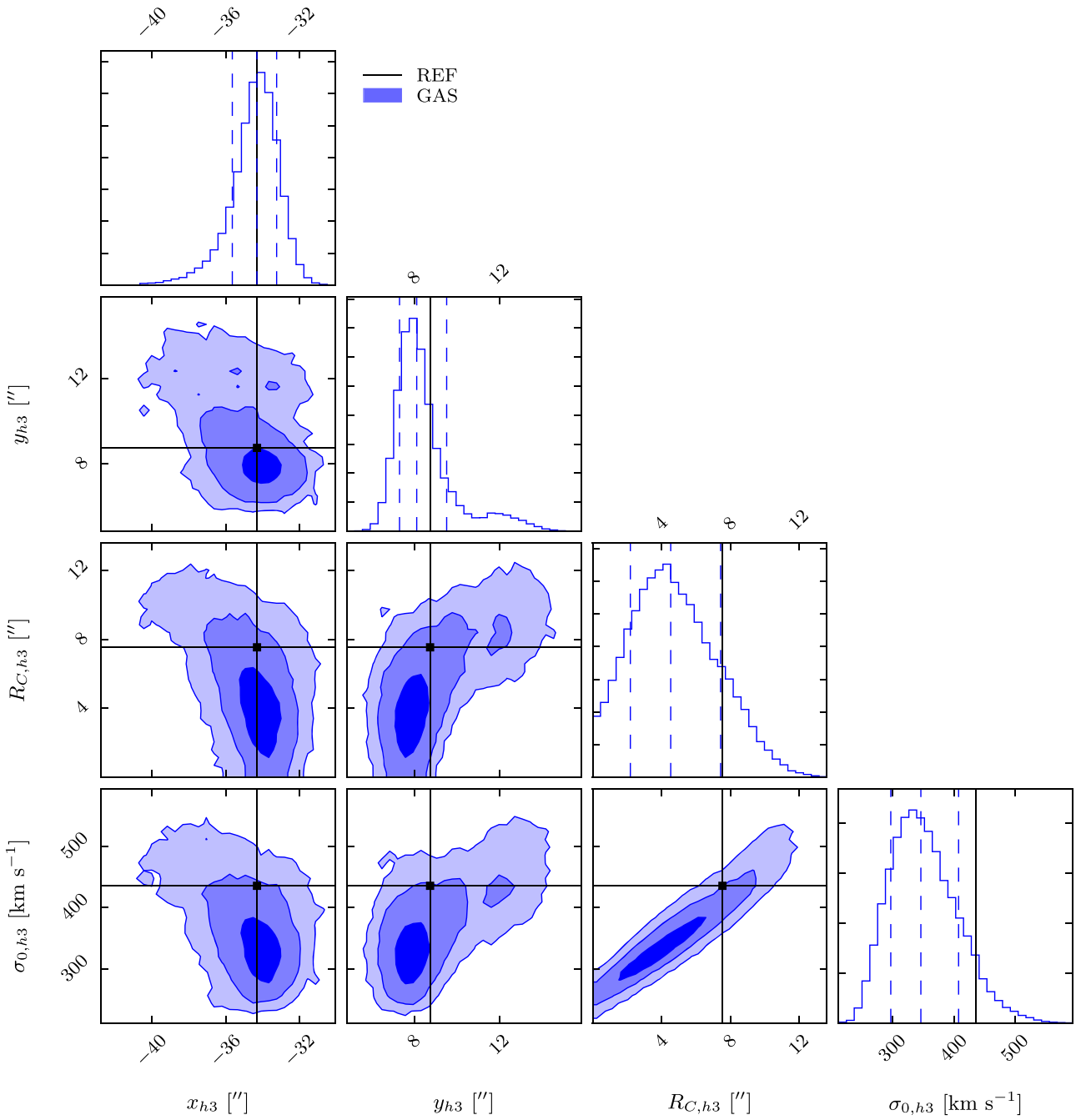

Figure 11. Posterior distributions of the values of the third main halo parameters derived from the strong-lensing model with the hot gas included separately (i.e., GAS model). Blue contours contain 39.3%, 86.5%, and 98.9% of the samples, while blue dashed lines in the 1D histograms show the 16th, 50th, and 84th percentiles. Black solid lines mark the median values of the reference model (i.e., REF model).

Moreover, relaxing the spherical assumption and choosing an ellipsoidal mass density distribution with two axes laying on the plane of the sky, the core and truncation radii can always be rescaled as follows:

$$\rho(x,\,y,\,z) = \frac{\rho_0}{\left(R_C^2 + \frac{x^2}{a^2} + \frac{y^2}{b^2} + \frac{z^2}{c^2}\right)\left(R_T^2 + \frac{x^2}{a^2} + \frac{y^2}{b^2} + \frac{z^2}{c^2}\right)} = \frac{\rho_0 c^4}{\left(R_C^2 c^2 + \frac{x^2c^2}{a^2} + \frac{y^2c^2}{b^2} + z^2\right)\left(R_T^2 c^2 + \frac{x^2c^2}{a^2} + \frac{y^2c^2}{b^2} + z^2\right)}$$
$$= \frac{\rho_0'}{(R_A'^2 + z^2)(R_B'2 + z^2)}. \tag{13}$$

From the substitutions in the last step and a comparison with Equations (2), (4), and (5), it is clear that the solution for an ellipsoidal dPIE will be the same as that for a spherical one, once the radii and densities are properly rescaled.

References

Akaike, H. 1974, ITAC, 19, 716
Bacon, R., Accardo, M., Adjali, L., et al. 2012, Msngr, 147, 4
Balestra, I., Mercurio, A., Sartoris, B., et al. 2016, ApJS, 224, 33
Balestra, I., Vanzella, E., Rosati, P., et al. 2013, A&A, 559, L9
Bender, R., Burstein, D., & Faber, S. M. 1992, ApJ, 399, 462
Biviano, A., Rosati, P., Balestra, I., et al. 2013, A&A, 558, A1
Boehringer, H., & Hensler, G. 1989, A&A, 215, 147
Broadhurst, T., Benítez, N., Coe, D., et al. 2005, ApJ, 621, 53
Caminha, G. B., Grillo, C., Rosati, P., et al. 2016, A&A, 587, A80
Caminha, G. B., Grillo, C., Rosati, P., et al. 2017, A&A, 600, A90
Cash, W. 1979, ApJ, 228, 939
Cavaliere, A., & Fusco-Femiano, R. 1976, A&A, 49, 137
Coe, D., Bradley, L., & Zitrin, A. 2015, ApJ, 800, 84
De Filippis, E., Sereno, M., Bautz, M. W., & Longo, G. 2005, ApJ, 625, 108
Diego, J. M., Broadhurst, T., Molnar, S. M., Lam, D., & Lim, J. 2015, MNRAS, 447, 3130
Donahue, M., Voit, G. M., Mahdavi, A., et al. 2014, ApJ, 794, 136
Elíasdóttir, Á, Limousin, M., Richard, J., et al. 2007, arXiv:0710.5636
Ettori, S. 2000, MNRAS, 311, 313
Ettori, S., Donnarumma, A., Pointecouteau, E., et al. 2013, SSRv, 177, 119
Faber, S. M., Dressler, A., Davies, R. L., Burstein, D., & Lynden-Bell, D. 1987, in Nearly Normal Galaxies: From the Planck Time to the Present, ed. S. M. Faber (New York: Springer), 175
Foreman-Mackey, D. 2016, The Journal of Open Source Software, 24 doi:10.21105/joss.00024
Grillo, C., Karman, W., Suyu, S. H., et al. 2016, ApJ, 822, 78
Grillo, C., Suyu, S. H., Rosati, P., et al. 2015, ApJ, 800, 38
Halkola, A., Seitz, S., & Pannella, M. 2006, MNRAS, 372, 1425
Harvey, D., Massey, R., Kitching, T., Taylor, A., & Tittley, E. 2015, Sci, 347, 1462
Hoag, A., Huang, K.-H., Treu, T., et al. 2016, ApJ, 831, 182
Jauzac, M., Clément, B., Limousin, M., et al. 2014, MNRAS, 443, 1549
Jauzac, M., Jullo, E., Eckert, D., et al. 2015, MNRAS, 446, 4132
Johnson, T. L., Sharon, K., Bayliss, M. B., et al. 2014, ApJ, 797, 48
Jullo, E., Kneib, J.-P., Limousin, M., et al. 2007, NJPh, 9, 447
Jullo, E., Natarajan, P., Kneib, J.-P., et al. 2010, Sci, 329, 924
Kalberla, P. M. W., Burton, W. B., Hartmann, D., et al. 2005, A&A, 440, 775
Karman, W., Caputi, K. I., Caminha, G. B., et al. 2017, A&A, 599, 28
Kassiola, A., & Kovner, I. 1993, ApJ, 417, 450
Klypin, A., Kravtsov, A. V., Valenzuela, O., & Prada, F. 1999, ApJ, 522, 82
Kneib, J.-P., & Natarajan, P. 2011, A&ARv, 19, 47
Laureijs, R., Amiaux, J., Arduini, S., et al. 2011, arXiv:1110.3193
Le Fèvre, O., Vettolani, G., Maccagni, D., et al. 2003, Proc. SPIE, 4834, 173
Limousin, M., Kneib, J.-P., & Natarajan, P. 2005, MNRAS, 356, 309
Limousin, M., Morandi, A., Sereno, M., et al. 2013, SSRv, 177, 155
Lotz, J. M., Koekemoer, A., Coe, D., et al. 2017, ApJ, 837, 97
Mann, A. W., & Ebeling, H. 2012, MNRAS, 420, 2120
Markevitch, M., Gonzalez, A. H., Clowe, D., et al. 2004, ApJ, 606, 819
Monna, A., Seitz, S., Balestra, I., et al. 2017, MNRAS, 466, 4094
Moore, B., Ghigna, S., Governato, F., et al. 1999, ApJL, 524, L19
Morandi, A., Limousin, M., Sayers, J., et al. 2012, MNRAS, 425, 2069
Oesch, P. A., Bouwens, R. J., Illingworth, G. D., et al. 2015, ApJ, 808, 104
Ogrean, G. A., van Weeren, R. J., Jones, C., et al. 2015, ApJ, 812, 153
Ogrean, G. A., van Weeren, R. J., Jones, C., et al. 2016, ApJ, 819, 113
Paraficz, D., Kneib, J.-P., Richard, J., et al. 2016, A&A, 594, A121
Postman, M., Coe, D., Benítez, N., et al. 2012, ApJS, 199, 25
Richard, J., Jauzac, M., Limousin, M., et al. 2014, MNRAS, 444, 268
Rosati, P., Balestra, I., Grillo, C., et al. 2014, Msngr, 158, 48
Rumsey, C., Olamaie, M., Perrott, Y. C., et al. 2016, MNRAS, 460, 569
Sarazin, C. L. 1988, X-ray Emission from Clusters of Galaxies (Cambridge: Cambridge Univ. Press)
Sarazin, C. L., & Bahcall, J. N. 1977, ApJS, 34, 451
Schwarz, G. 1978, AnSta, 6, 461
Sereno, M., Ettori, S., Meneghetti, M., et al. 2017, MNRAS, 467, 3801
Siegel, S. R., Sayers, J., Mahdavi, A., et al. 2016, arXiv:1612.05377
Springel, V., White, S. D. M., Tormen, G., & Kauffmann, G. 2001, MNRAS, 328, 726
Sutherland, R. S., & Dopita, M. A. 1993, ApJS, 88, 253
Suyu, S. H., & Halkola, A. 2010, A&A, 524, A94
Tormen, G. 1997, MNRAS, 290, 411
Umetsu, K., Sereno, M., Medezinski, E., et al. 2015, ApJ, 806, 207
van Weeren, R. J., Ogrean, G. A., Jones, C., et al. 2017, ApJ, 835, 197
Vanzella, E., Balestra, I., Gronke, M., et al. 2017, MNRAS, 465, 3803
Vikhlinin, A., Kravtsov, A., Forman, W., et al. 2006, ApJ, 640, 691
Voit, G. M. 2005, RvMP, 77, 207
Zitrin, A., Meneghetti, M., Umetsu, K., et al. 2013, ApJL, 762, L30